Azimuthally anisotropic emission of low-momentum direct photons in Au + Au collisions at √sNN = 200 GeV

(PHENIX Collaboration) Adare, A.; ...; Makek, Mihael; ...; Zou, L.

Azimuthally anisotropic emission of low-momentum direct photons in Au + Au collisions at $\sqrt{s_{NN}} = 200$ GeV

A. Adare,[13] S. Afanasiev,[32] C. Aidala,[42,46,47] N. N. Ajitanand,[67] Y. Akiba,[61,62] R. Akimoto,[12] H. Al-Bataineh,[55] J. Alexander,[67] M. Alfred,[25] H. Al-Ta'ani,[55] A. Angerami,[14] K. Aoki,[35,38,61] N. Apadula,[30,68] Y. Aramaki,[12,61] H. Asano,[38,61] E. C. Aschenauer,[7] E. T. Atomssa,[39,68] R. Averbeck,[68] T. C. Awes,[57] B. Azmoun,[7] V. Babintsev,[26] M. Bai,[6] G. Baksay,[20] L. Baksay,[20] N. S. Bandara,[46] B. Bannier,[68] K. N. Barish,[8] B. Bassalleck,[54] A. T. Basye,[1] S. Bathe,[5,8,62] V. Baublis,[60] C. Baumann,[7,48] S. Baumgart,[61] A. Bazilevsky,[7] M. Beaumier,[8] S. Beckman,[13] S. Belikov,[7,*] R. Belmont,[13,47,73] R. Bennett,[68] A. Berdnikov,[64] Y. Berdnikov,[64] A. A. Bickley,[13] D. S. Blau,[37] J. S. Bok,[54,55,77] K. Boyle,[62,68] M. L. Brooks,[42] J. Bryslawskyj,[5,8] H. Buesching,[7] V. Bumazhnov,[26] G. Bunce,[7,62] S. Butsyk,[42,54] C. M. Camacho,[42] S. Campbell,[14,30,68] P. Castera,[68] C.-H. Chen,[62,68] C. Y. Chi,[14] M. Chiu,[7] I. J. Choi,[27,77] J. B. Choi,[10,*] S. Choi,[66] R. K. Choudhury,[4] P. Christiansen,[44] T. Chujo,[72] P. Chung,[67] O. Chvala,[8] V. Cianciolo,[57] Z. Citron,[68,75] B. A. Cole,[14] M. Connors,[68] P. Constantin,[42] M. Csanád,[18] T. Csörgő,[76] T. Dahms,[68] S. Dairaku,[38,61] I. Danchev,[73] T. W. Danley,[56] K. Das,[21] A. Datta,[46,54] M. S. Daugherity,[1] G. David,[7] K. DeBlasio,[54] K. Dehmelt,[20,68] A. Denisov,[26] A. Deshpande,[62,68] E. J. Desmond,[7] K. V. Dharmawardane,[55] O. Dietzsch,[65] L. Ding,[30] A. Dion,[30,68] P. B. Diss,[45] J. H. Do,[77] M. Donadelli,[65] L. D'Orazio,[45] O. Drapier,[39] A. Drees,[68] K. A. Drees,[6] J. M. Durham,[42,68] A. Durum,[26] D. Dutta,[4] S. Edwards,[6,21] Y. V. Efremenko,[57] F. Ellinghaus,[13] T. Engelmore,[14] A. Enokizono,[41,57,61,63] H. En'yo,[61,62] S. Esumi,[72] K. O. Eyser,[7,8] B. Fadem,[49] N. Feege,[68] D. E. Fields,[54] M. Finger,[9] M. Finger, Jr.,[9] F. Fleuret,[39] S. L. Fokin,[37] Z. Fraenkel,[75,*] J. E. Frantz,[56,68] A. Franz,[7] A. D. Frawley,[21] K. Fujiwara,[61] Y. Fukao,[61] T. Fusayasu,[51] K. Gainey,[1] C. Gal,[68] P. Gallus,[15] P. Garg,[3,68] A. Garishvili,[70] I. Garishvili,[41,70] H. Ge,[68] F. Giordano,[27] A. Glenn,[13,41] H. Gong,[68] X. Gong,[67] M. Gonin,[39] Y. Goto,[61,62] R. Granier de Cassagnac,[39] N. Grau,[2,14] S. V. Greene,[73] M. Grosse Perdekamp,[27,62] T. Gunji,[12] L. Guo,[42] H.-Å. Gustafsson,[44,*] T. Hachiya,[24,61,62] J. S. Haggerty,[7] K. I. Hahn,[19] H. Hamagaki,[12] J. Hamblen,[70] H. F. Hamilton,[1] R. Han,[59] S. Y. Han,[19] J. Hanks,[14,68] E. P. Hartouni,[41] S. Hasegawa,[31] T. O. S. Haseler,[22] K. Hashimoto,[61,63] E. Haslum,[44] R. Hayano,[12] X. He,[22] M. Heffner,[41] T. K. Hemmick,[68] T. Hester,[8] J. C. Hill,[30] M. Hohlmann,[20] R. S. Hollis,[8] W. Holzmann,[14] K. Homma,[24] B. Hong,[36] T. Horaguchi,[24,72] Y. Hori,[12] D. Hornback,[70] T. Hoshino,[24] N. Hotvedt,[30] J. Huang,[7] S. Huang,[73] T. Ichihara,[61,62] R. Ichimiya,[61] J. Ide,[49] H. Iinuma,[35] Y. Ikeda,[61,72] K. Imai,[31,38,61] J. Imrek,[17] M. Inaba,[72] A. Iordanova,[8] D. Isenhower,[1] M. Ishihara,[61] T. Isobe,[12,61] M. Issah,[73] A. Isupov,[32] D. Ivanishchev,[60] B. V. Jacak,[68] M. Javani,[22] M. Jezghani,[22] J. Jia,[7,67] X. Jiang,[42] J. Jin,[14] B. M. Johnson,[7,22] K. S. Joo,[50] D. Jouan,[58] D. S. Jumper,[1,27] F. Kajihara,[12] S. Kametani,[61] N. Kamihara,[62] J. Kamin,[68] S. Kanda,[12] S. Kaneti,[68] B. H. Kang,[23] J. H. Kang,[77] J. S. Kang,[23] J. Kapustinsky,[42] K. Karatsu,[38,61] M. Kasai,[61,63] D. Kawall,[46,62] M. Kawashima,[61,63] A. V. Kazantsev,[37] T. Kempel,[30] J. A. Key,[54] V. Khachatryan,[68] A. Khanzadeev,[60] K. M. Kijima,[24] B. I. Kim,[36] C. Kim,[36] D. H. Kim,[50] D. J. Kim,[33] E. Kim,[66] E.-J. Kim,[10] G. W. Kim,[19] H. J. Kim,[77] K.-B. Kim,[10] M. Kim,[66] S. H. Kim,[77] Y.-J. Kim,[27] Y. K. Kim,[23] B. Kimelman,[49] E. Kinney,[13] K. Kiriluk,[13] Á. Kiss,[18] E. Kistenev,[7] R. Kitamura,[12] J. Klatsky,[21] D. Kleinjan,[8] P. Kline,[68] T. Koblesky,[13] L. Kochenda,[60] Y. Komatsu,[12,35] B. Komkov,[60] M. Konno,[72] J. Koster,[27] D. Kotchetkov,[54,56] D. Kotov,[60,64] A. Kozlov,[75] A. Král,[15] A. Kravitz,[14] F. Krizek,[33] G. J. Kunde,[42] K. Kurita,[61,63] M. Kurosawa,[61,62] Y. Kwon,[77] G. S. Kyle,[55] R. Lacey,[67] Y. S. Lai,[14] J. G. Lajoie,[30] A. Lebedev,[30] B. Lee,[23] D. M. Lee,[42] J. Lee,[19,69] K. Lee,[66] K. B. Lee,[36] K. S. Lee,[36] S. Lee,[77] S. H. Lee,[68] S. R. Lee,[10] M. J. Leitch,[42] M. A. L. Leite,[65] M. Leitgab,[27] E. Leitner,[73] B. Lenzi,[65] B. Lewis,[68] X. Li,[11] P. Liebing,[62] S. H. Lim,[77] L. A. Linden Levy,[13] T. Liška,[15] A. Litvinenko,[32] H. Liu,[42,55] M. X. Liu,[42] B. Love,[73] R. Luechtenborg,[48] D. Lynch,[7] C. F. Maguire,[73] Y. I. Makdisi,[6] M. Makek,[75,78] A. Malakhov,[32] M. D. Malik,[54] A. Manion,[68] V. I. Manko,[37] E. Mannel,[7,14] Y. Mao,[59,61] H. Masui,[72] S. Masumoto,[12,35] F. Matathias,[14] M. McCumber,[13,42,68] P. L. McGaughey,[42] D. McGlinchey,[13,21] C. McKinney,[27] N. Means,[68] A. Meles,[55] M. Mendoza,[8] B. Meredith,[27] Y. Miake,[72] T. Mibe,[35] A. C. Mignerey,[45] P. Mikeš,[9,29] K. Miki,[61,72] A. Milov,[7,75] D. K. Mishra,[4] M. Mishra,[3] J. T. Mitchell,[7] Y. Miyachi,[61,71] S. Miyasaka,[61,71] S. Mizuno,[61,72] A. K. Mohanty,[4] S. Mohapatra,[67] P. Montuenga,[27] H. J. Moon,[50] T. Moon,[77] Y. Morino,[12] A. Morreale,[8] D. P. Morrison,[7,†] S. Motschwiller,[49] T. V. Moukhanova,[37] T. Murakami,[38,61] J. Murata,[61,63] A. Mwai,[67] T. Nagae,[38] S. Nagamiya,[35,61] K. Nagashima,[24] J. L. Nagle,[13,‡] M. Naglis,[75] M. I. Nagy,[18,76] I. Nakagawa,[61,62] H. Nakagomi,[61,72] Y. Nakamiya,[24] K. R. Nakamura,[38,61] T. Nakamura,[35,61] K. Nakano,[61,71] C. Nattrass,[70] A. Nederlof,[49] P. K. Netrakanti,[4] J. Newby,[41] M. Nguyen,[68] M. Nihashi,[24,61] T. Niida,[72] S. Nishimura,[12] R. Nouicer,[7,62] T. Novák,[34,76] N. Novitzky,[33,68] A. S. Nyanin,[37] E. O'Brien,[7] S. X. Oda,[12] C. A. Ogilvie,[30] M. Oka,[72] K. Okada,[62] Y. Onuki,[61] J. D. Orjuela Koop,[13] J. D. Osborn,[47] A. Oskarsson,[44] M. Ouchida,[24,61] K. Ozawa,[12,35] R. Pak,[7] V. Pantuev,[28,68] V. Papavassiliou,[55] B. H. Park,[23] I. H. Park,[19,69] J. Park,[66] J. S. Park,[66] S. Park,[66] S. K. Park,[36] W. J. Park,[36] S. F. Pate,[55] L. Patel,[22] M. Patel,[30] H. Pei,[30] J.-C. Peng,[27] H. Pereira,[16] D. V. Perepelitsa,[7,13,14] G. D. N. Perera,[55] V. Peresedov,[32] D.Yu. Peressounko,[37] J. Perry,[30] R. Petti,[7,68] C. Pinkenburg,[7] R. Pinson,[1] R. P. Pisani,[7] M. Proissl,[68] M. L. Purschke,[7] A. K. Purwar,[42] H. Qu,[1,22] J. Rak,[33] A. Rakotozafindrabe,[39] B. J. Ramson,[47] I. Ravinovich,[75] K. F. Read,[57,70] K. Reygers,[48] D. Reynolds,[67] V. Riabov,[53,60] Y. Riabov,[60,64] E. Richardson,[45] T. Rinn,[30] D. Roach,[73] G. Roche,[43,*] S. D. Rolnick,[8] M. Rosati,[30] C. A. Rosen,[13] S. S. E. Rosendahl,[44] P. Rosnet,[43] Z. Rowan,[5] J. G. Rubin,[47] P. Rukoyatkin,[32] P. Ružička,[29] B. Sahlmueller,[48,68] N. Saito,[35] T. Sakaguchi,[7] K. Sakashita,[61,71] H. Sako,[31] V. Samsonov,[53,60] M. Sano,[72] S. Sano,[12,74] M. Sarsour,[22] S. Sato,[31,35] T. Sato,[72] S. Sawada,[35] B. Schaefer,[73] B. K. Schmoll,[70] K. Sedgwick,[8] J. Seele,[13] R. Seidl,[27,61,62] A.Yu. Semenov,[30] A. Sen,[22,30,70] R. Seto,[8] P. Sett,[4] A. Sexton,[45] D. Sharma,[68,75] I. Shein,[26] T.-A. Shibata,[61,71] K. Shigaki,[24] M. Shimomura,[30,52,72] K. Shoji,[38,61] P. Shukla,[4] A. Sickles,[7,27] C. L. Silva,[30,42,65] D. Silvermyr,[44,57] C. Silvestre,[16] K. S. Sim,[36]

B. K. Singh,[3] C. P. Singh,[3] V. Singh,[3] M. Slunečka,[9] M. Snowball,[42] R. A. Soltz,[41] W. E. Sondheim,[42] S. P. Sorensen,[70] I. V. Sourikova,[7] N. A. Sparks,[1] P. W. Stankus,[57] E. Stenlund,[44] M. Stepanov,[46,55,*] A. Ster,[76] S. P. Stoll,[7] T. Sugitate,[24] A. Sukhanov,[7] T. Sumita,[61] J. Sun,[68] J. Sziklai,[76] E. M. Takagui,[65] A. Takahara,[12] A. Taketani,[61,62] R. Tanabe,[72] Y. Tanaka,[51] S. Taneja,[68] K. Tanida,[38,61,62,66] M. J. Tannenbaum,[7] S. Tarafdar,[3,73,75] A. Taranenko,[53,67] P. Tarján,[17] E. Tennant,[55] H. Themann,[68] T. L. Thomas,[54] R. Tieulent,[22] A. Timilsina,[30] T. Todoroki,[61,72] M. Togawa,[38,61] A. Toia,[68] L. Tomášek,[29] M. Tomášek,[15,29] H. Torii,[24] C. L. Towell,[1] R. Towell,[1] R. S. Towell,[1] I. Tserruya,[75] Y. Tsuchimoto,[12,24] T. Tsuji,[12] C. Vale,[7,30] H. Valle,[73] H. W. van Hecke,[42] M. Vargyas,[18,76] E. Vazquez-Zambrano,[14] A. Veicht,[14,27] J. Velkovska,[73] R. Vértesi,[17,76] A. A. Vinogradov,[37] M. Virius,[15] A. Vossen,[27] V. Vrba,[15,29] E. Vznuzdaev,[60] X. R. Wang,[55,62] D. Watanabe,[24] K. Watanabe,[72] Y. Watanabe,[61,62] Y. S. Watanabe,[12,35] F. Wei,[30,55] R. Wei,[67] J. Wessels,[48] A. S. White,[47] S. N. White,[7] D. Winter,[14] S. Wolin,[27] J. P. Wood,[1] C. L. Woody,[7] R. M. Wright,[1] M. Wysocki,[13,57] B. Xia,[56] W. Xie,[62] L. Xue,[22] S. Yalcin,[68] Y. L. Yamaguchi,[12,61,68] K. Yamaura,[24] R. Yang,[27] A. Yanovich,[26] J. Ying,[22] S. Yokkaichi,[61,62] J. H. Yoo,[36] I. Yoon,[66] Z. You,[42,59] G. R. Young,[57] I. Younus,[40,54] H. Yu,[55,59] I. E. Yushmanov,[37] W. A. Zajc,[14] A. Zelenski,[6] C. Zhang,[57] S. Zhou,[11] L. Zolin,[32] and L. Zou[8]

(PHENIX Collaboration)

[1]*Abilene Christian University, Abilene, Texas 79699, USA*

[2]*Department of Physics, Augustana University, Sioux Falls, South Dakota 57197, USA*

[3]*Department of Physics, Banaras Hindu University, Varanasi 221005, India*

[4]*Bhabha Atomic Research Centre, Bombay 400 085, India*

[5]*Baruch College, City University of New York, New York, New York 10010, USA*

[6]*Collider-Accelerator Department, Brookhaven National Laboratory, Upton, New York 11973-5000, USA*

[7]*Physics Department, Brookhaven National Laboratory, Upton, New York 11973-5000, USA*

[8]*University of California-Riverside, Riverside, California 92521, USA*

[9]*Charles University, Ovocný trh 5, Praha 1, 116 36 Prague, Czech Republic*

[10]*Chonbuk National University, Jeonju 561-756, Korea*

[11]*Science and Technology on Nuclear Data Laboratory, China Institute of Atomic Energy, Beijing 102413, People's Republic of China*

[12]*Center for Nuclear Study, Graduate School of Science, University of Tokyo, 7-3-1 Hongo, Bunkyo, Tokyo 113-0033, Japan*

[13]*University of Colorado, Boulder, Colorado 80309, USA*

[14]*Columbia University, New York, New York 10027, USA and Nevis Laboratories, Irvington, New York 10533, USA*

[15]*Czech Technical University, Zikova 4, 166 36 Prague 6, Czech Republic*

[16]*Dapnia, CEA Saclay, F-91191 Gif-sur-Yvette, France*

[17]*Debrecen University, Egyetem tér 1, H-4010 Debrecen, Hungary*

[18]*ELTE, Eötvös Loránd University, H-1117 Budapest, Pázmány P. s. 1/A, Hungary*

[19]*Ewha Womans University, Seoul 120-750, Korea*

[20]*Florida Institute of Technology, Melbourne, Florida 32901, USA*

[21]*Florida State University, Tallahassee, Florida 32306, USA*

[22]*Georgia State University, Atlanta, Georgia 30303, USA*

[23]*Hanyang University, Seoul 133-792, Korea*

[24]*Hiroshima University, Kagamiyama, Higashi-Hiroshima 739-8526, Japan*

[25]*Department of Physics and Astronomy, Howard University, Washington, D.C. 20059, USA*

[26]*IHEP Protvino, State Research Center of Russian Federation, Institute for High Energy Physics, Protvino 142281, Russia*

[27]*University of Illinois at Urbana-Champaign, Urbana, Illinois 61801, USA*

[28]*Institute for Nuclear Research of the Russian Academy of Sciences, prospekt 60-letiya Oktyabrya 7a, Moscow 117312, Russia*

[29]*Institute of Physics, Academy of Sciences of the Czech Republic, Na Slovance 2, 182 21 Prague 8, Czech Republic*

[30]*Iowa State University, Ames, Iowa 50011, USA*

[31]*Advanced Science Research Center, Japan Atomic Energy Agency, 2-4 Shirakata Shirane, Tokai-mura, Naka-gun, Ibaraki-ken 319-1195, Japan*

[32]*Joint Institute for Nuclear Research, 141980 Dubna, Moscow Region, Russia*

[33]*Helsinki Institute of Physics and University of Jyväskylä, P.O. Box 35, FI-40014 Jyväskylä, Finland*

[34]*Károly Róberts University College, H-3200 Gyöngyös, Mátrai út 36, Hungary*

[35]*KEK, High Energy Accelerator Research Organization, Tsukuba, Ibaraki 305-0801, Japan*

[36]*Korea University, Seoul 136-701, Korea*

[37]*National Research Center "Kurchatov Institute", Moscow 123098, Russia*

[38]*Kyoto University, Kyoto 606-8502, Japan*

[39]*Laboratoire Leprince-Ringuet, Ecole Polytechnique, CNRS-IN2P3, Route de Saclay, F-91128 Palaiseau, France*

[40]*Physics Department, Lahore University of Management Sciences, Lahore 54792, Pakistan*

[41]*Lawrence Livermore National Laboratory, Livermore, California 94550, USA*

[42]*Los Alamos National Laboratory, Los Alamos, New Mexico 87545, USA*

[43]*LPC, Université Blaise Pascal, CNRS-IN2P3, Clermont-Fd, 63177 Aubiere Cedex, France*

[44]*Department of Physics, Lund University, Box 118, SE-221 00 Lund, Sweden*

[45]*University of Maryland, College Park, Maryland 20742, USA*
[46]*Department of Physics, University of Massachusetts, Amherst, Massachusetts 01003-9337, USA*
[47]*Department of Physics, University of Michigan, Ann Arbor, Michigan 48109-1040, USA*
[48]*Institut für Kernphysik, University of Muenster, D-48149 Muenster, Germany*
[49]*Muhlenberg College, Allentown, Pennsylvania 18104-5586, USA*
[50]*Myongji University, Yongin, Kyonggido 449-728, Korea*
[51]*Nagasaki Institute of Applied Science, Nagasaki-shi, Nagasaki 851-0193, Japan*
[52]*Nara Women's University, Kita-uoya Nishi-machi, Nara 630-8506, Japan*
[53]*National Research Nuclear University, MEPhI, Moscow Engineering Physics Institute, Moscow 115409, Russia*
[54]*University of New Mexico, Albuquerque, New Mexico 87131, USA*
[55]*New Mexico State University, Las Cruces, New Mexico 88003, USA*
[56]*Department of Physics and Astronomy, Ohio University, Athens, Ohio 45701, USA*
[57]*Oak Ridge National Laboratory, Oak Ridge, Tennessee 37831, USA*
[58]*IPN-Orsay, Univ. Paris-Sud, CNRS/IN2P3, Université Paris-Saclay, Boîte Postale 1, F-91406 Orsay, France*
[59]*Peking University, Beijing 100871, People's Republic of China*
[60]*PNPI, Petersburg Nuclear Physics Institute, Gatchina, Leningrad Region 188300, Russia*
[61]*RIKEN Nishina Center for Accelerator-Based Science, Wako, Saitama 351-0198, Japan*
[62]*RIKEN BNL Research Center, Brookhaven National Laboratory, Upton, New York 11973-5000, USA*
[63]*Physics Department, Rikkyo University, 3-34-1 Nishi-Ikebukuro, Toshima, Tokyo 171-8501, Japan*
[64]*Saint Petersburg State Polytechnic University, St. Petersburg 195251, Russia*
[65]*Universidade de São Paulo, Instituto de Física, Caixa Postal 66318, São Paulo CEP 05315-970, Brazil*
[66]*Department of Physics and Astronomy, Seoul National University, Seoul 151-742, Korea*
[67]*Chemistry Department, Stony Brook University, SUNY, Stony Brook, New York 11794-3400, USA*
[68]*Department of Physics and Astronomy, Stony Brook University, SUNY, Stony Brook, New York 11794-3800, USA*
[69]*Accelerator and Medical Instrumentation Engineering Lab, SungKyunKwan University, 53 Myeongnyun-dong, 3-ga, Jongno-gu, Seoul 110-745, Korea*
[70]*University of Tennessee, Knoxville, Tennessee 37996, USA*
[71]*Department of Physics, Tokyo Institute of Technology, Oh-okayama, Meguro, Tokyo 152-8551, Japan*
[72]*Center for Integrated Research in Fundamental Science and Engineering, University of Tsukuba, Tsukuba, Ibaraki 305, Japan*
[73]*Vanderbilt University, Nashville, Tennessee 37235, USA*
[74]*Waseda University, Advanced Research Institute for Science and Engineering, 17 Kikui-cho, Shinjuku-ku, Tokyo 162-0044, Japan*
[75]*Weizmann Institute, Rehovot 76100, Israel*
[76]*Institute for Particle and Nuclear Physics, Wigner Research Centre for Physics, Hungarian Academy of Sciences (Wigner RCP, RMKI) H-1525 Budapest 114, P.O. Box 49, Budapest, Hungary*
[77]*Yonsei University, IPAP, Seoul 120-749, Korea*
[78]*University of Zagreb, Faculty of Science, Department of Physics, Bijenička 32, HR-10002 Zagreb, Croatia*
(Received 5 October 2015; published 6 December 2016)

The PHENIX experiment at the BNL Relativistic Heavy Ion Collider has measured second- and third-order Fourier coefficients of the azimuthal distributions of direct photons emitted at midrapidity in Au + Au collisions at $\sqrt{s_{NN}} = 200$ GeV for various collision centralities. Combining two different analysis techniques, results were obtained in the transverse momentum range of $0.4 < p_T < 4.0$ GeV/c. At low p_T the second-order coefficients, v_2, are similar to the ones observed in hadrons. Third-order coefficients, v_3, are nonzero and almost independent of centrality. These new results on v_2 and v_3, combined with previously published results on yields, are compared to model calculations that provide yields and asymmetries in the same framework. Those models are challenged to explain simultaneously the observed large yield and large azimuthal anisotropies.

DOI: 10.1103/PhysRevC.94.064901

I. INTRODUCTION

Direct photons emerging from relativistic heavy-ion collisions have long been considered an important probe of the entire evolution of the colliding system [1]. At almost all known or conjectured stages of the collision there are processes producing photons. Unlike hadronic observables that mostly encode the state of the medium at freeze-out, photons are emitted at all times throughout the rapid evolution of the heavy-ion collision and leave the interaction region unmodified. Thus by measuring direct photons one has access to information about the properties and dynamics of the medium integrated over space and time. The measurement of direct photons is challenging due to a large background of photons from the vacuum decay of final state hadrons (π^0, η, ω, etc.).

*Deceased.
†PHENIX Co-spokesperson: morrison@bnl.gov
‡PHENIX Co-spokesperson: jamie.nagle@colorado.edu

The PHENIX experiment at the BNL Relativistic Heavy Ion Collider reported large direct photon yields [2] with strong centrality dependence [3] and significant azimuthal anisotropy or "elliptic flow" [4]. Particularly surprising is the discovery of large azimuthal anisotropy for direct photons [4], which is comparable to that observed for hadrons [5]. Preliminary results from the CERN Large Hadron Collider [6,7] indicate similar direct photon yields and anisotropies. The observation of large azimuthal anisotropy combined with observations published earlier that the direct photon yields themselves are large [2,3] contradicts several existing interpretations where the large yields are provided at the very early production stage, when the temperature of the system is highest but the collective flow including azimuthal asymmetry is negligible. Conversely, the observed large anisotropy suggests that photon production occurs at very late stages of the collision when the collective flow of the system is fully developed, while the temperature and the corresponding thermal photon emission rates are already lower. Indeed, theoretical models have great difficulty to simultaneously describe the observed yields and anisotropy. This failure, colloquially called "the direct photon puzzle," triggered a large amount of theoretical work, new models, and insights [8–31].

In this article we present new, more precise results on the azimuthal anisotropy of direct photon emission from 200-GeV Au + Au collisions recorded in 2007 and 2010 by the PHENIX experiment. Results include second- and third-order Fourier components of azimuthal distributions (v_2 and v_3, respectively) measured over a transverse momentum range extended down to 0.4 GeV/c. The new data, together with published results on yields, are compared to some of the more recent model calculations.

The article is organized as follows. In Sec. II we describe the experiment, the data set, the way events are selected and categorized, and the two methods by which photons are measured. In Sec. III the steps needed to determine the direct photon v_2 and v_3 and their uncertainties are described, and the final results are presented. In Sec. IV the results are compared to a few models treating yields and azimuthal asymmetries in a consistent framework. Section V summarizes our findings.

II. EXPERIMENTAL SETUP AND PHOTON MEASUREMENTS

In the PHENIX experiment photons are detected by two substantially different techniques. The first technique uses external conversion of photons as described in detail in Ref. [3]. This method provides a high-purity photon sample with good momentum resolution, but requires large statistics due to the few percent conversion probability and reduced acceptance. Therefore the p_T range is limited. The second technique is a traditional calorimetric measurement of photons similar to Ref. [4], but with higher statistics. For photons identified by either technique, the azimuthal anisotropy is extracted with the event plane (EP) method. Here we give a brief summary of the PHENIX detector systems and a short description of the two analyses.

A. Event selection and centrality determination

Data from 200-GeV Au + Au collisions were recorded with a minimum-bias (MB) trigger based on the signal in the beam-beam counters (BBCs) [32], which are located around the beampipe at $3.1 < |\eta| < 3.9$ and cover the full azimuth. The MB trigger requires at least two hits in each of the two BBCs (north and south) as well as a reconstructed vertex from the time-of-flight difference between the two sides. The efficiency of the MB trigger is $92.3 \pm 0.4(\text{stat}) \pm 1.6(\text{sys})\%$.

Collision centrality is calculated as percentiles of the total charge distribution in the north and south BBCs. The centrality determination is based on percentiles of the total charge seen in the north and south BBCs and takes into account small shifts in η coverage due to variations of the collision's z vertex.

B. Inclusive photons via external conversion

External conversion photons are reconstructed from 2.6×10^9 MB $\sqrt{s_{NN}} = 200$ GeV Au + Au events recorded during the 2010 data taking period. The event vertex in this data set was $|z| < 10$ cm to ensure that the magnetic field would be sufficiently uniform. The same sample was previously used in Ref. [3] to determine direct photon yield and its centrality dependence, where details of this analysis can be found. In the rest of this article this sample is referred to as "conversion photons."

Photons convert to e^+e^- pairs in the readout plane of the hadron blind detector (HBD) [33], which is located at ~60 cm radial distance from the collision vertex and corresponds to ~3% X_0, where X_0 is the radiation length. The electron and positron from the photon conversion are tracked through the PHENIX central tracking detectors [34]. The azimuthal direction ϕ and the momentum p are reconstructed from the drift-chamber information, while the polar angle of each track is determined by a point measurement in the innermost pad-chamber and the collision vertex. High-efficiency electron identification cuts are used to reduce the hadron contamination in the sample. Light above a minimum threshold in the ring-imaging Čerenkov detector [35] and a matching cluster of energy E in the electromagnetic calorimeter (EMCal) [36] such that $E > 0.15$ GeV and $E/p > 0.5$, where p is the momentum, are required. The EMCal comprises two calorimeter types: six sectors of lead scintillator sampling calorimeter (PbSc) and two sectors of lead glass Čerenkov calorimeter (PbGl). The typical energy resolution of the PbSc is $\delta E/E = 8.1\%/\sqrt{E(\text{GeV})} \oplus 2.1\%$, and that of the PbGl is $\delta E/E = 5.9\%/\sqrt{E(\text{GeV})} \oplus 0.8\%$. The energy resolution, just like the photon identification efficiency, depends on centrality and its (small) effect is corrected for using simulated photon showers embedded into real events.

All remaining tracks with $p_T > 0.2$ GeV/c, are combined into pairs. Conversion photons are identified by analyzing the invariant mass of the pairs. The default tracking in PHENIX assumes that each track originates at the collision vertex. Thus, if the e^+e^- pair comes from a conversion of a real photon in the HBD readout plane, the momenta will be mismeasured and a finite mass, in this case about $m_{ee} \sim 12$ MeV/c^2, will be reconstructed. Conversely, if the momenta are recalculated assuming the HBD readout plane as the origin, the invariant

mass is close to zero. Through a simultaneous cut on both mass calculations a sample of photon conversions with a purity of 99% is obtained down to $p_T = 0.4$ GeV/c [3]. The remaining 1% of pairs are mostly from the π^0 Dalitz decays. The effect on the inclusive photon v_n is estimated to be smaller than 1%.

C. Inclusive photons and π^0s via the calorimeter

The PHENIX EMCal is the principal detector in the calorimetric analysis, which is performed in a similar way as in Ref. [4]. The v_2 and v_3 are measured simultaneously for inclusive photons and π^0s. A total of 4.4×10^9 MB Au + Au events from the 2007 data-taking period are analyzed. The event vertex in this sample was $|z| < 30$ cm.

Photon candidates in the EMCal are clusters above a threshold energy of 0.2 GeV that pass a shower shape cut as well as a charged particle veto cut by the pad chamber PC3 immediately in front of the EMCal. However, photon candidates with less than 1 GeV energy are only used to reconstruct π^0, but are not included in the inclusive photon sample of the calorimeter. As described in Ref. [37], the remaining hadron contamination was estimated by comparing GEANT simulations, verified with actual data. The π^0 is measured via the 2γ decay channel, with a cut on the energy asymmetry of the two photons $\alpha = \frac{|E_1-E_2|}{E_1+E_2} < 0.8$. For each p_T bin the number of reconstructed π^0s is taken as the integral of the two-photon invariant mass distribution, with the combinatorial background subtracted by the mixed event method [38]. The signal to background ratio at $1.0 < p_T < 1.5$ GeV/c is 0.1, rapidly improving with increasing p_T.

For the inclusive photon measurement it is important to restrict the measurement to a region where the residual contamination from misidentified hadrons is small. Therefore, in the inclusive photon sample only clusters with $E > 1$ GeV are considered. On the other hand the inclusive (and direct) photon results presented here have an upper range of 4 GeV/c, which is far from the threshold where two decay photons from a π^0 can merge in the calorimeter. Within this p_T range a purity of larger than 95% is achieved. The largest contamination of the photon sample results from antineutrons, which are not removed by the charge particle veto but deposit significant energy through annihilation. The systematic uncertainty from particle identification of photons is estimated by varying both the shower shape cut (five different settings) and, independently, by applying or omitting the charged particle veto cut. Results from all cut variations are then fully corrected. The deviation between results is 3%–4%, which is quoted as systematic uncertainty on the inclusive photon yield.

D. Event plane determination

PHENIX has different detector systems to establish the EP, which cover different pseudorapidity (η) ranges: the outer and inner reaction plane detector (RxNO, $1 < |\eta| < 1.5$, RxNI, $1.5 < |\eta| < 2.8$.), the muon piston calorimeters (MPCS, $-3.7 < \eta < 3.1$, MPCN, $3.1 < \eta < 3.9$.), and the BBC ($3.1 < |\eta| < 3.9$.). All these detectors cover the full 2π azimuth and are sufficiently separated in η such that we do not expect autocorrelations between the event plane determination and the photon production asymmetry measured. The RxNI and RXNO are scintillation counter systems with a 2-cm Pb converter that makes them sensitive to photons in addition to charged particles. While these photons contribute to the determination of the event plane, note that they are separated at least $\Delta\eta = 0.7$ from the central region, which is where the photon v_2 and v_3 are measured.

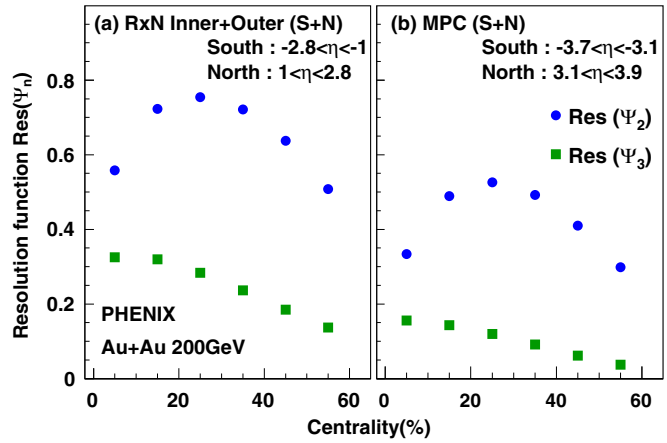

FIG. 1. Event plane resolution as a function of centrality for the RxN(I+O) detector (a) used for the final results in this article and (b) for the MPC detector used to cross-check the results.

The results in this article are obtained using the event planes measured by the combination of the RxNI and the RxNO [39]. Due to the large rapidity coverage this combination has the best resolution. The resolution Res(Ψ_n) is measured with the two-subevent method [40]. The resolution for the RxN and MPC detectors is shown in Fig. 1. The final results are cross-checked by using the other detectors for the event plane determination. Despite the significant difference in resolution the measured direct photon anisotropies are consistent, within the systematic uncertainties.

III. DIRECT PHOTON v_2 AND v_3

The photon anisotropy is measured via the coefficients of a Fourier decomposition of the azimuthal distributions of photons with respect to the event plane [40]:

$$\frac{dN}{d(\phi - \Psi_k)} \propto 1 + \sum_n \{v_{kn} \cos[n(\phi - \Psi_k)]\}, \qquad (1)$$

where ϕ is the azimuthal angle of the photon, Ψ_k is the orientation of the k^{th} event plane for a given event, and v_{kn} are the n^{th} coefficients with respect to the k^{th} event plane. In our analysis we made and explicitly tested the assumption that the second- and third-order event planes are uncorrelated, which allows us to ignore the $k \neq n$ terms and to introduce the notation v_2 and v_3 for the case $k = n$; i.e., in the rest of the article we use $v_2 \equiv v_{22}$ and $v_3 \equiv v_{33}$.

The determination of the direct photon v_2 and v_3 proceeds in three steps: (i) v_2 and v_3 are determined for the conversion photon sample (Sec. II B) and for the calorimeter photon sample (Sec. II C) with respect to the event plane (Sec. II D). We refer to these coefficients as inclusive photon v_2^{inc} and

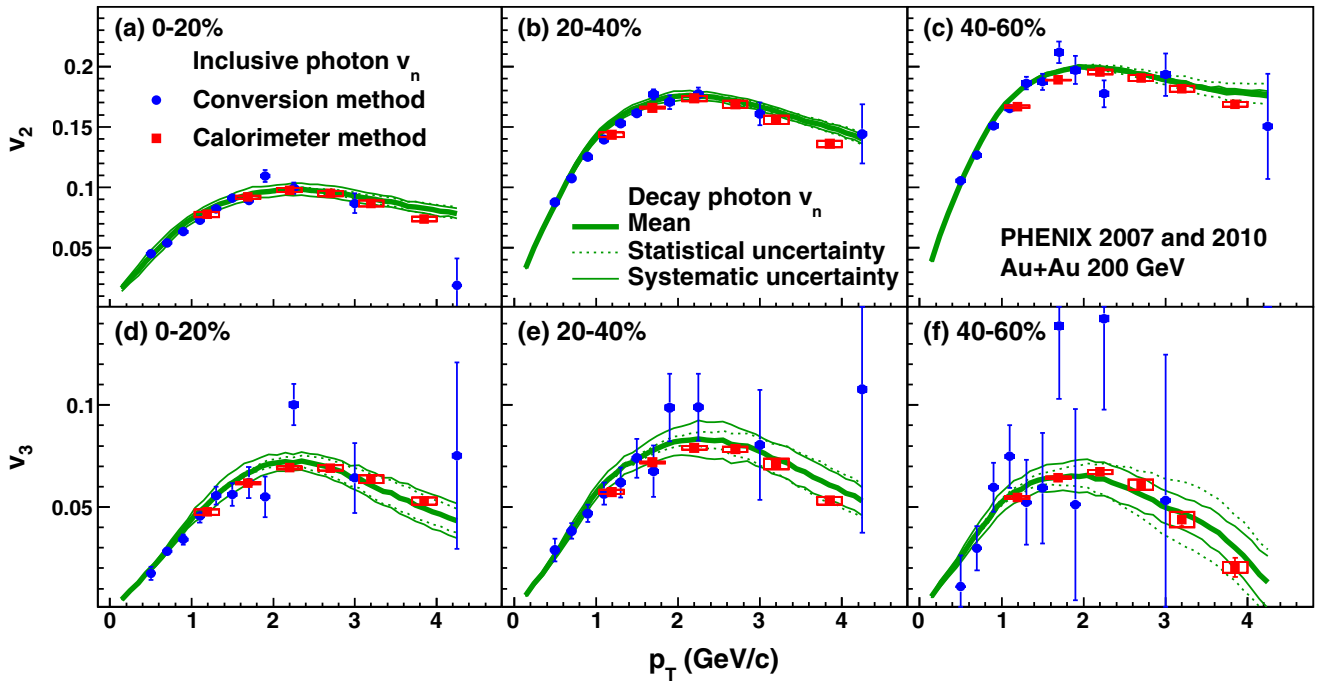

FIG. 2. Inclusive photon v_2 and v_3 at midrapidity ($|\eta| < 0.35$) for Au + Au collisions at $\sqrt{s_{NN}} = 200$ GeV in different centrality bins 0%–20% (a,d), 20%–40% (b,e), and 40%–60% (c,f) with the event plane estimated with the reaction plane detector ($1 < |\eta| < 2.8$.). The data from the external conversion method are shown as solid circles and from the calorimeter method as solid squares. The error bars (boxes) around the data points are statistical (systematic) uncertainties. Also shown are the calculated decay photon v_2 and v_3 (thick solid line) along with the statistical (dotted line) and systematic (light solid line) uncertainties resulting from uncertainties on the input data. An additional systematic uncertainty due to the finite event plane resolution is not shown (see Table I), because it is common to all v_n measurements.

$v_3^{\rm inc}$. In the second step (ii), the decay photon $v_2^{\rm dec}$ and $v_3^{\rm dec}$ are estimated, i.e., the anisotropy resulting from the decays of hadrons to photons. It is calculated based on v_2, v_3, and yields measured for charged and neutral pions; contributions from heavier mesons are taken into account using proper scaling (see Sec. III B). As a final step (iii), the direct photon v_2 and v_3 are calculated statistically through a subtraction of the results from steps (i) and (ii) weighted by the ratio R_γ, the ratio of the yields of direct photons to the yield of photons from hadron decays [see Eq. (7)].

A. Inclusive photon v_2 and v_3

The inclusive photon v_2 and v_3 are measured with respect to the event plane. We employ two methods to determine these coefficients. For each photon the azimuthal angular difference $(\phi - \Psi_k)$, with $k = 2$ and 3, is calculated. In the first method the coefficients are determined as the event ensemble average for individual bins in photon p_T and centrality:

$$v_n = \langle \cos\{n(\phi - \Psi_n)\}\rangle / \mathrm{Res}(\Psi_n). \quad (2)$$

Here $\mathrm{Res}(\Psi_n)$ is the resolution function that accounts for the finite event plane resolution (see Fig. 1).

In the second method the azimuthal distribution of photons in a given p_T and centrality bin is fitted as

$$\frac{dN}{d(\phi - \Psi_n)} = N_0\{1 + 2v_n' \cos[n(\phi - \Psi_n)]\}, \quad (3)$$

$$v_n = v_n'/\mathrm{Res}(\Psi_n). \quad (4)$$

This is Eq. (1) for the case $k = n$ and neglecting all $k \neq n$ terms. The measured values of v_2 and v_3 (v_2', v_3') need to be corrected for the event plane resolution.

In the conversion photon method the quoted v_n values come from the average cosine method, while in the calorimeter analysis the quoted v_n values are the average of the results obtained with the two methods. The difference between the two methods is less than 1%. The results for the inclusive photon v_2 and v_3 are shown in Fig. 2. Both measurements agree in the region where they overlap.

B. Decay photon v_2 and v_3

About 80%–90% of the inclusive photons come from decays of neutral mesons and exhibit an anisotropy with respect to the event plane that results from the anisotropy of the parent mesons [4]. To estimate this contribution we use measured yields and anisotropy for charged and neutral pions; v_n for heavier mesons is obtained by KE_T scaling as described below. The yields of mesons used here are the same as those used for the measurement of R_γ in Ref. [3].

The v_2 and v_3 for pions are determined by combining data from different measurements of charged and neutral pion v_2 and v_3. The π^0 v_2 has been published in Ref. [41] but the measurement has been repeated in this analysis to check the consistency of the results. The method to count the number of

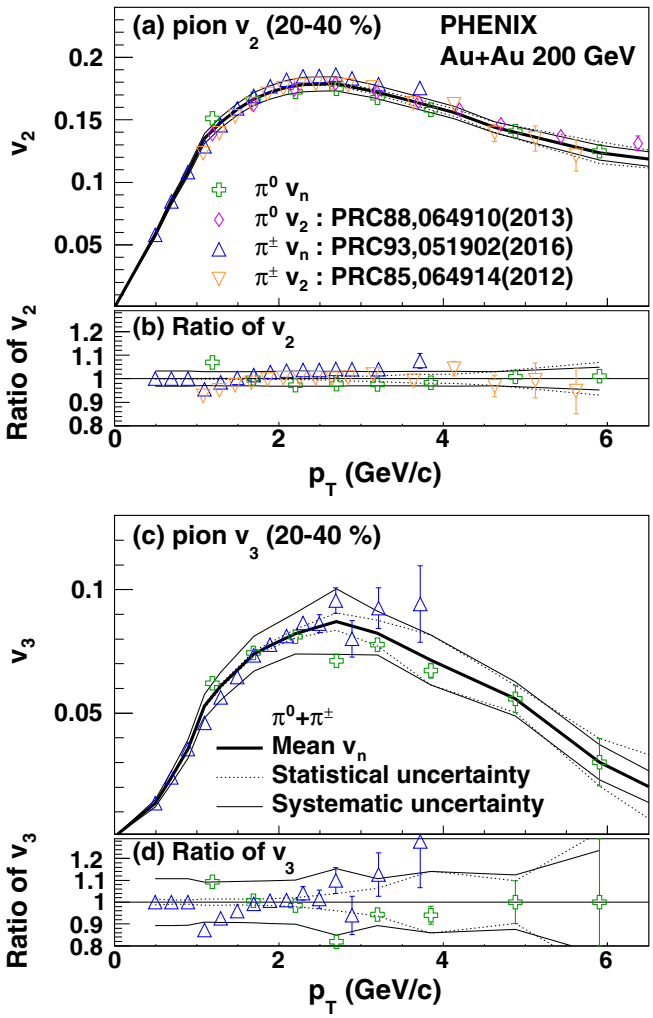

FIG. 3. Top panels: Charged and neutral pion v_2 (a) and v_3 (c) for the 20%–40% centrality class, including previously published results. The averaged values used in our analysis are shown as a thick solid line together with the estimated statistical (dotted line) and systematic (light solid line) uncertainties. Bottom panels: Ratio of the measured v_2 (b) and v_3 (d) values to the averaged values.

π^0s in any p_T bin is briefly described in Sec. II C. To obtain v_2 (v_3) for each p_T the number of reconstructed π^0s is extracted in six 15° (10°) wide bins of the azimuthal angle $\Delta\Phi = \Phi - \Psi_n$, where Φ is the azimuth of the π^0 and Ψ_n is the second-order (third-order) event plane (see Sec. II D). These distributions of the raw π^0 counts vs $\Delta\Phi$ are then fitted as described in Sec. III A to obtain v_2 and v_3 for π^0. Note that because the individual π^0s are not identified, the average cosine method [40] is not applicable.

These data are combined with $\pi^\pm$ data in the p_T range 0.5 to 4 GeV/c [42]. For v_2 we also use $\pi^\pm$ data from Ref. [43]. For the centrality class 20%–40% these data are compiled in Fig. 3. We interpolate the data, weighted by their statistical and systematic uncertainties, to obtain an average value v_n for pions as a function of p_T. The result of this averaging procedure, including our estimate of the systematic uncertainties, is also shown in Fig. 3.

For the heavier mesons, η, ω, ρ, and η', the v_n is derived from the v_n of the pions by scaling with the kinetic energy [42,44]:

$$v_n^{\text{meson}}(KE_T) = v_n^{\pi}(KE_T), \tag{5}$$

where

$$KE_T = m_T - m = \sqrt{p_T^2 + m^2} - m, \tag{6}$$

where m is the mass of the corresponding meson.

The yields of the heavier mesons are determined from the π^0 yields at $p_T = 5\,\text{GeV}/c$ using the following ratios: $\eta/\pi^0 = 0.46 \pm 0.060$, $\omega/\pi^0 = 0.83 \pm 0.12$, $\rho/\pi^0 = 1.00 \pm 0.300$, and $\eta'/\pi^0 = 0.25 \pm 0.075$. Below $p_T = 2$ GeV/c KE_T scaling is only an extrapolation for the η yields. Therefore, we also applied a blast-wave fit, and the difference is included in the systematic uncertainties. Note that the blast-wave fit results in a lower η yield at small p_T, increasing the direct photon yield and its v_2 and v_3. The meson yields, momentum spectra, and v_n are used to simulate mesons that are then decayed to all decay chains including photons. From the simulation we calculate the decay photon v_n^{dec} using Eq. (2) with $\text{Res}(\Psi_n) = 1$, because the event plane is known in the simulation. The only source of systematic uncertainty on v_n^{dec} is the uncertainty of the measured π^0 v_2 and v_3, and the resulting decay photon v_2 and v_3, derived from it. The resulting v_n^{dec} is compared to the inclusive photon v_n in Fig. 2. We find that the decay photon v_n and the inclusive photon v_n are similar. This was already observed for v_2 in Ref. [4], but is now also found for v_3. Given that a finite direct photon yield has already been established [2,3], the similarity of v_3^{inc} and v_3^{dec} implies a large direct photon v_3, as is shown in the next section.

C. Direct photon v_2 and v_3

The v_2 and v_3 for direct photons are extracted from the measured inclusive photon v_n^{inc}, the decay photon v_n^{dec}, discussed in the previous sections, and the ratio of the inclusive to decay photon yield R_γ measured in Ref. [3]. The procedure was introduced in Ref. [4]:

$$v_n^{\text{dir}} = \frac{R_\gamma v_n^{\text{inc}} - v_n^{\text{dec}}}{R_\gamma - 1}. \tag{7}$$

We reproduce R_γ from Ref. [3] with statistical and systematic uncertainties in Fig. 4.

All systematic uncertainties on the individual contributions on v_n^{dir} are summarized in Table I. Uncertainties that are uncorrelated between data points are called Type A, those that are correlated are Type B, and uncertainties that change all points by a common multiplicative factor are called Type C. Uncertainties on R_γ are common for v_2 and v_3 and for the conversion and calorimeter methods. For photon and pion v_n measurements with PHENIX, the orientation of the event planes, i.e., Ψ_n, is determined with the same detectors using the same algorithms. Thus the systematic uncertainty on the event plane determination is common for all v_2 (v_3) measurements. The uncertainties on the decay photon v_n are common to the conversion and calorimeter methods. The systematic uncertainty on v_n^{inc} is independent

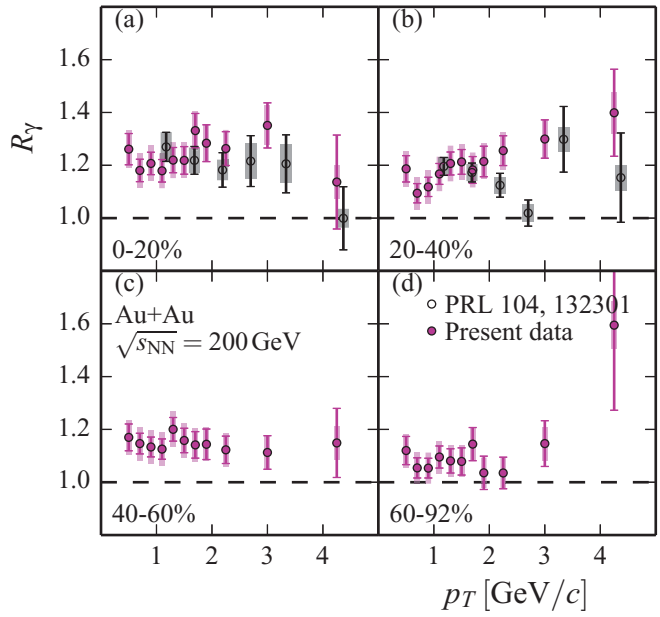

FIG. 4. The inclusive over decay photon ratio R_γ used in the current analysis. Present data means the results published in Ref. [3].

for the two methods and mostly reflects the different purity of >95% compared to >99% for the calorimeter and conversion methods, respectively.

TABLE I. Summary of systematic uncertainties on the input to the measurement of $v_n^{\rm dir}$, where the R_γ is from Ref. [3] and the $v_n^{\rm inc}$ and $v_n^{\rm dec}$ indicate "inclusive" and "decay" photons, respectively. The values are quoted for $p_T < 3$ GeV/c, although most do not vary with p_T, as can be seen from Figs. 2 and 3. The uncertainties on the $v_n^{\rm dec}$ due to the statistical uncertainty of the input data are uncorrelated between data points (type A); they are included in the statistical errors on the final results. Type B uncertainties are correlated in p_T; i.e., they can vary with p_T but only smoothly in the quoted range. Type C uncertainties change $v_n^{\rm dir}$ for all p_T by a constant multiplicative factor. The systematic uncertainties on v_2 and v_3 are typical values.

Input	Source	Centralities			Type
		0%–20%	20%–40%	40%–60%	
R_γ		5.5%	5.5%	5.5%	B
$v_2^{\rm inc}$	Conversion method	<1%	<1%	<1%	B
	Calorimeter method	4%	3%	4%	B
$v_2^{\rm dec}$	Meson v_2 (stat)	<1%	<1%	<1%	A
	π^0 v_2 (sys)	5%	3%	2%	B
	η,ω v_2 (sys)	<1%	<1%	<1%	B
	Event plane	3%	3%	3%	C
$v_3^{\rm inc}$	Conversion method	<1%	<1%	<1%	B
	Calorimeter method	5%	7%	10%	B
$v_3^{\rm dec}$	Meson v_3 (stat)	1%	2%	4%	A
	π^0 v_3 (sys)	11%	11%	11%	B
	η,ω v_3 (sys)	~1%	~1%	~1%	B
	Event plane	6%	7%	18%	C

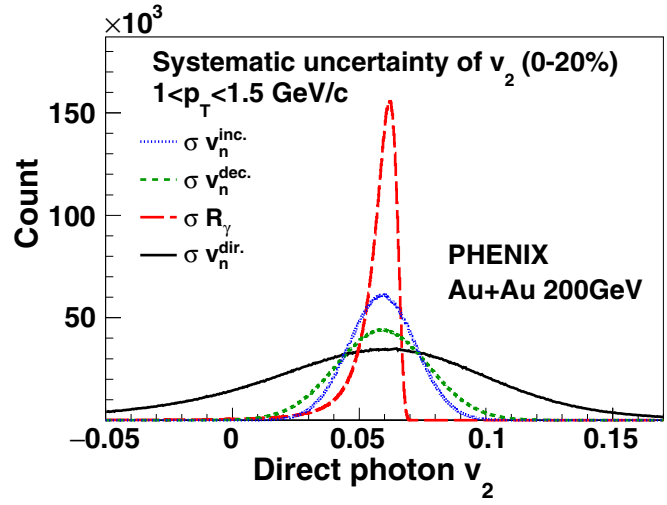

FIG. 5. This example shows the direct photon $v_2^{\rm dir}$ measured via the calorimeter method with the event plane estimated by the reaction plane detector ($1 < |\eta| < 2.8$) in the 0%–20% centrality bin. Each of the various dashed curves indicate the probability distribution of the $v_2^{\rm dir}$ result due to the variation of a single term in Eq. (7). While varying $v_2^{\rm inc}$ and $v_2^{\rm dec}$ alone leaves the uncertainty on $v_2^{\rm dir}$ Gaussian, varying R_γ results in strongly asymmetric shapes. The black solid curve shows the result when all uncertainties are taken into account simultaneously.

Using Gaussian error propagation, the statistical and systematic uncertainties would be calculated as

$$\sigma^2_{v_n^{\rm dir}} = \left(\frac{R_\gamma}{R_\gamma - 1}\right)^2 \sigma^2_{v_n^{\rm inc}} + \left(\frac{1}{R_\gamma - 1}\right)^2 \times \sigma^2_{v_n^{\rm dec}} + \left(\frac{v_n^{\rm dec} - v_n^{\rm inc}}{R_\gamma - 1}\right)^2 \sigma^2_{R_\gamma} + \sigma^2_{EP}. \quad (8)$$

Except for the case $v_n^{\rm inc} = v_n^{\rm dec}$, there is a nonlinear dependence on R_γ that, combined with uncertainties of 20%–30% on $(R_\gamma - 1)$, results in asymmetric uncertainties, which are not described by Eq. (8). In particular, for the case $v_n^{\rm dec} > v_n^{\rm inc}$ the uncertainties on $v_n^{\rm dec}$ and $v_n^{\rm inc}$ are amplified if R_γ is small.

We estimate these asymmetric uncertainties by modeling a probability distribution for possible values of $v_n^{\rm dir}$ using the statistical and systematic uncertainties on $v_n^{\rm inc}$, $v_n^{\rm dec}$, R_γ, and the event plane resolution. We assume that the individual statistical and systematic uncertainties follow Gaussian probability distributions. The probability distribution for $v_n^{\rm dir}$ is then determined by generating many combinations of $v_n^{\rm inc}$, $v_n^{\rm dec}$, and R_γ. Figure 5 shows one example of a probability distribution based on the systematic uncertainties on the calorimeter measurement for 0%–20% centrality and $1 < p_T < 1.5$ GeV/c. In Fig. 5 the effect of the uncertainty of only $v_n^{\rm inc}$, $v_n^{\rm dec}$, or R_γ, are plotted separately. The asymmetry due to the uncertainty of R_γ is clearly visible.

Probability distributions based on statistical (including type A systematics) and systematic uncertainties are determined for each $v_n^{\rm dir}$ data point in p_T and centrality and for both analyses. The central value for each data point was calculated using Eq. (7). We note that the peak or median of the probability distributions used to determine the statistical and systematic

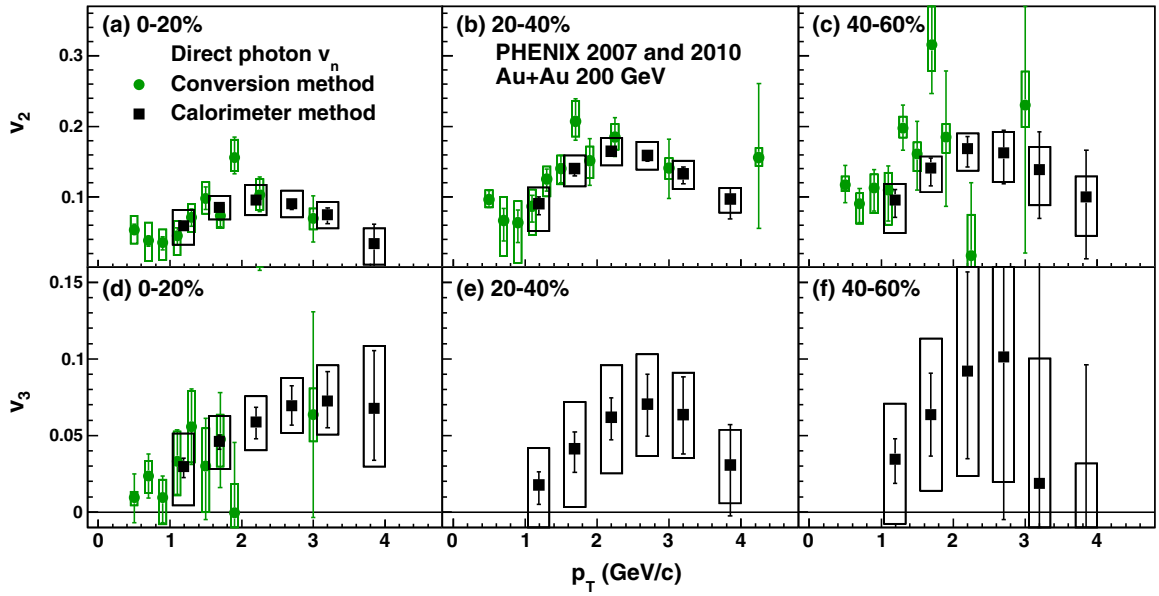

FIG. 6. Direct photon v_2 and v_3 at midrapidity ($|\eta| < 0.35$), for different centralities, measured with the conversion method (solid circles, green) and the calorimeter method (solid squares, black). The event plane was determined with the reaction plane detector ($1 < |\eta| < 2.8$). The error bars (boxes) around the data points are statistical (systematic) uncertainties.

uncertainties agrees with the calculated central value to better than the symbol size. From each distribution we calculate the lower and upper bounds on the uncertainty by integrating from $\pm\infty$ to a v_n for which the integrated probability reaches 15.9%. These values bracket a 68% probability range for v_n and are quoted as upper and lower statistical and systematic uncertainties on the final result.

The final results for the direct photon v_2 and v_3, including statistical and systematic uncertainties as outlined above, are shown in Fig. 6 for three centralities and separately for the two analysis methods. For the conversion method v_3 is shown only for the highest centrality bin; the statistical fluctuations preclude any meaningful measurement in the more peripheral bins. The data and their uncertainties are shown in Tables II and III.

The two analysis techniques are very different but the results agree well in the overlap region, and they are also consistent with the results published earlier [4]. The direct photon v_2 centrality dependence, both in trend and magnitude, is quite similar to the observed pion v_2. The third-order coefficients v_3 are consistent with no centrality dependence.

IV. COMPARISONS TO MODELS

As already mentioned, the essence of the "direct photon puzzle" is that current theoretical scenarios have difficulties explaining the large direct photon yield and azimuthal asymmetries at the same time. This is illustrated by a recent state-of-the-art calculation of viscous hydrodynamic calculation of photon emission with fluctuating initial density profiles and standard thermal rates [17], which falls significantly short in describing yield and v_2. Over the past few years many new ideas have been proposed to resolve this puzzle, including nonequilibrium effects [19,24,26,28], enhanced early emission due to large magnetic fields [15,25,27], enhanced emission at hadronization [31], and modifications of the formation time and initial conditions [20,22,23].

In this subsection we compare our results to a subset of the models which (i) consider thermal radiation from the quark-gluon plasma (QGP) and HG (hadron gas) plus additional proposed sources, (ii) have a complete model for the space-time evolution, and (iii) calculate absolute yields and v_2. For the comparison we use the data for the 20%–40% centrality class, and note that the comparison leads to similar conclusions for the other centrality bins. While none of the models describe all aspects of the available data, they are representative of how different theories are trying to cope with the challenge.

First, we compare the data to the "fireball" scenario originally calculated in Ref. [12]. The model includes perturbative quantum chromodynamics (pQCD), QGP, and HG contributions, with the instantaneous rates convoluted with a fireball expansion profile. The basic parameter is the initial transverse acceleration of the fireball, a_T. The prompt photon component is estimated in two ways. The first variant is a parametrization of the photon yields measured in $p + p$ by the PHENIX experiment [45] (labeled as "primordial 1"); the second is an x_t-scaling motivated parametrization (labeled as "primordial 2"), modified with the empirical factor $K = 2.5$ to match the measured data at high p_T (above 4 GeV/c). The yield calculation includes thermal yields from the QGP with $T_0 = 350$ MeV and from the hadronic phase. Different from an earlier version of the model, chemical equilibrium prior to kinetic freeze-out is no longer assumed. This results in a large enhancement in photon production in the later hadronic stages via processes like meson annihilation (for instance, $\pi + \rho \to \pi + \gamma$). With an initial transverse acceleration of $a_T = 0.12\,c^2/\mathrm{fm}$ and $\tau \approx 15\,\mathrm{fm}/c$ fireball lifetime, 100 MeV freeze-out temperature, and $\beta_s = 0.77$ surface velocity, the observed

TABLE II. Direct photon v_2 for the indicated centrality bins for the two methods used. Uncertainties are shown separately as upper and lower.

Centrality	Method	$\langle p_T \rangle$ (GeV/c)	v_2	Statistical uncert.	Systematic uncert.
0%–20%	Conversion photon	0.50	0.0531	+0.0084, −0.0076	+0.0200, −0.0187
		0.70	0.0387	+0.0070, −0.0087	+0.0252, −0.0291
		0.90	0.0357	+0.0080, −0.0104	+0.0185, −0.0246
		1.10	0.0456	+0.0105, −0.0135	+0.0208, −0.0277
		1.30	0.0713	+0.0116, −0.0128	+0.0185, −0.0207
		1.50	0.0979	+0.0162, −0.0153	+0.0227, −0.0214
		1.70	0.0735	+0.0148, −0.0160	+0.0157, −0.0173
		1.90	0.1560	+0.0291, −0.0229	+0.0254, −0.0192
		2.25	0.1034	+0.0247, −0.0243	+0.0223, −0.0215
		3.00	0.0699	+0.0316, −0.0338	+0.0140, −0.0155
		4.25	−0.3534	+0.8077, −0.1197	+0.1149, −0.1831
	Calorimeter	1.19	0.0591	+0.0038, −0.0058	+0.0225, −0.0266
		1.69	0.0852	+0.0029, −0.0035	+0.0163, −0.0170
		2.20	0.0957	+0.0046, −0.0050	+0.0214, −0.0218
		2.70	0.0903	+0.0074, −0.0078	+0.0186, −0.0190
		3.20	0.0747	+0.0098, −0.0122	+0.0177, −0.0189
		3.85	0.0339	+0.0282, −0.0430	+0.0218, −0.0298
20%–40%	Conversion photon	0.50	0.0964	+0.0125, −0.0113	+0.0133, −0.0113
		0.70	0.0668	+0.0173, −0.0289	+0.0336, −0.0485
		0.90	0.0640	+0.0178, −0.0281	+0.0308, −0.0555
		1.10	0.0866	+0.0155, −0.0217	+0.0240, −0.0403
		1.30	0.1251	+0.0146, −0.0170	+0.0178, −0.0240
		1.50	0.1405	+0.0182, −0.0202	+0.0185, −0.0227
		1.70	0.2074	+0.0316, −0.0269	+0.0291, −0.0212
		1.90	0.1511	+0.0314, −0.0342	+0.0207, −0.0245
		2.25	0.1846	+0.0279, −0.0273	+0.0186, −0.0174
		3.00	0.1412	+0.0407, −0.0431	+0.0137, −0.0160
		4.25	0.1561	+0.1048, −0.0992	+0.0133, −0.0121
	Calorimeter	1.19	0.0902	+0.0097, −0.0151	+0.0236, −0.0377
		1.69	0.1403	+0.0066, −0.0104	+0.0185, −0.0248
		2.20	0.1649	+0.0046, −0.0056	+0.0188, −0.0202
		2.70	0.1592	+0.0071, −0.0083	+0.0189, −0.0200
		3.20	0.1327	+0.0098, −0.0136	+0.0190, −0.0216
		3.85	0.0972	+0.0155, −0.0277	+0.0153, −0.0192
40%–60%	Conversion photon	0.50	0.1173	+0.0272, −0.0252	+0.0117, −0.0086
		0.70	0.0905	+0.0214, −0.0266	+0.0149, −0.0280
		0.90	0.1128	+0.0261, −0.0327	+0.0192, −0.0349
		1.10	0.1101	+0.0338, −0.0444	+0.0243, −0.0473
		1.30	0.1978	+0.0325, −0.0313	+0.0163, −0.0138
		1.50	0.1608	+0.0465, −0.0508	+0.0168, −0.0244
		1.70	0.3154	+0.0943, −0.0687	+0.0771, −0.0366
		1.90	0.1848	+0.0943, −0.0969	+0.0184, −0.0224
		2.25	0.0173	+0.1036, −0.1478	+0.0584, −0.1188
		3.00	0.2305	+0.2262, −0.1954	+0.0473, −0.0310
		4.25	−0.0043	+0.4198, −0.2826	+0.0466, −0.0920
	Calorimeter	1.19	0.0960	+0.0147, −0.0247	+0.0226, −0.0462
		1.69	0.1412	+0.0139, −0.0255	+0.0162, −0.0334
		2.20	0.1687	+0.0172, −0.0258	+0.0212, −0.0313
		2.70	0.1624	+0.0323, −0.0427	+0.0302, −0.0405
		3.20	0.1388	+0.0539, −0.0657	+0.0319, −0.0487
		3.85	0.0999	+0.0670, −0.0788	+0.0290, −0.0533

low-p_T photon yields are recovered within systematic uncertainties, but underpredict the data [12]. In Fig. 7 the data are compared to the most recent updated "fireball" scenario shown in Ref. [18], which includes a calculation with ideal hydrodynamics with finite initial flow at thermalization and enhanced yields around the chemical freeze-out temperature T_c that improves the description of the data. The direct photon v_2 has its maximum at about the same p_T in both theory and

TABLE III. Direct photon v_3 for the indicated centrality bins for the two methods used. Uncertainties are shown separately as upper and lower.

Centrality	Method	$\langle p_T \rangle$ (GeV/c)	v_3	Statistical uncert.	Systematic uncert.
0%–20%	Conversion photon	0.50	0.0094	+0.0155, −0.0163	+0.0039, −0.0052
		0.70	0.0237	+0.0142, −0.0146	+0.0099, −0.0111
		0.90	0.0094	+0.0143, −0.0163	+0.0119, −0.0173
		1.10	0.0333	+0.0204, −0.0218	+0.0193, −0.0223
		1.30	0.0558	+0.0247, −0.0247	+0.0233, −0.0233
		1.50	0.0299	+0.0314, −0.0346	+0.0246, −0.0301
		1.70	0.0476	+0.0305, −0.0317	+0.0161, −0.0177
		1.90	−0.0006	+0.0461, −0.0535	+0.0189, −0.0265
		2.25	0.2094	+0.0657, −0.0516	+0.0461, −0.0299
		3.00	0.0637	+0.0672, −0.0672	+0.0172, −0.0174
		4.25	0.2753	+0.4140, −0.4118	+0.1492, −0.0765
	Calorimeter	1.19	0.0298	+0.0055, −0.0073	+0.0214, −0.0256
		1.69	0.0461	+0.0040, −0.0053	+0.0166, −0.0182
		2.20	0.0587	+0.0096, −0.0110	+0.0170, −0.0185
		2.70	0.0696	+0.0129, −0.0129	+0.0180, −0.0180
		3.20	0.0726	+0.0191, −0.0175	+0.0231, −0.0221
		3.85	0.0677	+0.0380, −0.0332	+0.0408, −0.0378
20%–40%	Calorimeter	1.19	0.0178	+0.0085, −0.0127	+0.0240, −0.0343
		1.69	0.0415	+0.0108, −0.0154	+0.0304, −0.0381
		2.20	0.0619	+0.0128, −0.0146	+0.0339, −0.0365
		2.70	0.0703	+0.0198, −0.0206	+0.0326, −0.0336
		3.20	0.0637	+0.0244, −0.0256	+0.0274, −0.0284
		3.85	0.0308	+0.0265, −0.0331	+0.0228, −0.0250
40%–60%	Calorimeter	1.19	0.0346	+0.0131, −0.0157	+0.0362, −0.0422
		1.69	0.0638	+0.0271, −0.0273	+0.0497, −0.0494
		2.20	0.0920	+0.0651, −0.0567	+0.0780, −0.0676
		2.70	0.1011	+0.1224, −0.1028	+0.0973, −0.0793
		3.20	0.0187	+0.1580, −0.1476	+0.0823, −0.0877
		3.85	−0.0430	+0.1421, −0.1289	+0.0751, −0.0938

data. The v_2 calculated in the original fireball scenario [12] under predicts the measured one. The radial boost hardens the photons from the HG and in this way increases v_2 as well, but the calculation still falls short of the measurement. v_3 is currently not calculated in this model.

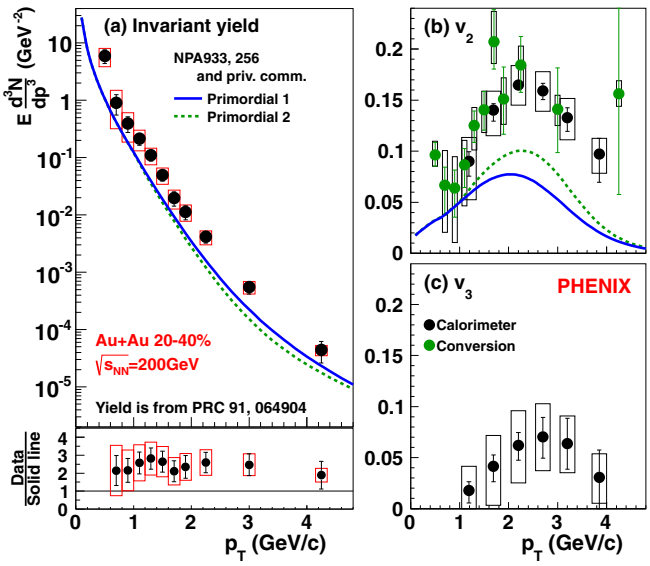

FIG. 7. Comparison of the direct photon yields [3] and v_2 with the fireball model [18]. The two curves for v_2 correspond to two different parametrizations of the prompt photon component. See text for details.

Second, in Fig. 8 the data are compared to three calculations evaluated with the hydrodynamical background as described in Refs. [46,47]. The first calculation, labeled "QGP w/viscous," was evaluated using the AMY photon emission rate in the high-temperature (QGP) region and included viscous corrections to the photon emission rates [21,48] due to both bulk and shear viscosities. The same calculation without the viscous corrections corresponds to the curve labeled "QGP, w/o viscous." Once viscous corrections are included, v_2 drops by more than 50% at 3 GeV/c, while the yield decreases just by ∼10%. The third curve, labeled "semi-QGP, w/o viscous," shows the consequence of including the effect of confinement on the photon emission rate, as computed in the semi-QGP approach [14]. The utilization of the semi-QGP photon rates at high temperatures suppresses the spectrum, but does not change the v_n significantly. This is a consequence of the small contribution of QGP photons to the thermal photon v_2, which is dominantly produced at temperatures around and smaller than the confinement temperature. The prompt photon contributions in all three calculations are evaluated within the pQCD framework.

Third, we compare the data with PHSD (parton-hadron-string dynamics), a microscopic transport model [13]. In

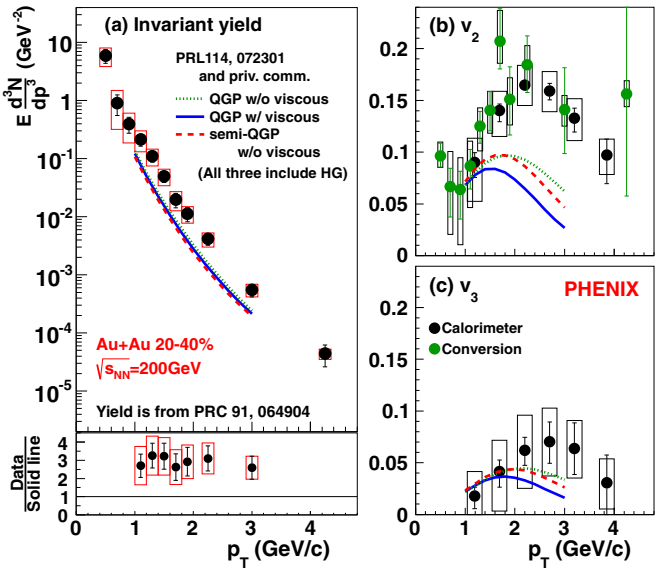

FIG. 8. Comparison of the direct photon yields and v_2 and v_3 with a hydrodynamical model [46,47] calculated under three different assumptions including the "semi-QGP" scenario [14].

addition to the traditional QGP and HG sources (resonance decays) this model includes late stage meson-meson and meson-baryon Bremsstrahlung, which enhances the yield at the lowest p_T substantially and increases v_2 by almost 50% in the p_T <3 GeV/c region (see Fig. 2 in Ref. [13]). Contributions from photonic decays of ϕ and a_1 are also included, because these are not subtracted in the measurement. After all other sources are added, the direct photon spectrum is very well reproduced below 3 GeV/c, but v_2 underpredicts the measured values. Also, the p_T where v_2 reaches its maximum is under predicted. In Fig. 9 the data are compared to the latest PHSD model calculation [49] that included additional photon

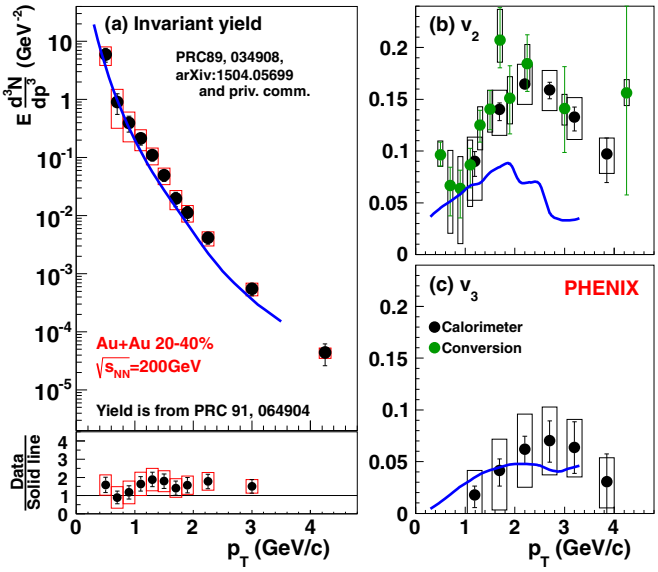

FIG. 9. Comparison of the direct photon yields and v_2 with the PHSD model [13,49].

production channels in the hadronic phase and improved the Bremsstrahlung calculation. The model also provides v_3. It is positive and consistent with the data within uncertainties.

Explaining the large yield and strong flow simultaneously requires significant improvements in quantifying the contributions from the late stage QGP and HG interactions. Even deeper insight on both the photon sources and the time profile of the system may be necessary to further improve the models. Future measurements of more differential quantities will help to distinguish and quantify the individual photon sources.

V. SUMMARY AND CONCLUSIONS

The PHENIX experiment at the Relativistic Heavy Ion Collider measured second- and third-order Fourier coefficients of the azimuthal distributions of direct photons emitted at midrapidity in $\sqrt{s_{NN}} = 200$ GeV Au + Au collisions, for various collision centralities. Two different and independent analyses are used to determine the inclusive photon yield. The external conversion photon measurement allows one to extend the p_T range down to 0.4 GeV/c compared to 1.0 GeV/c for the calorimetric measurement. In the overlap region the two results are consistent. The v_2 measurements are also consistent with earlier published results, while v_3 is published for the first time.

Both the direct photon v_2 and v_3 are found to be large. The v_2 exhibits a clear centrality-dependence, while v_3 is consistent with no centrality dependence. At all centralities, the direct photon v_2 is similar in magnitude to the hadron v_2 for p_T <3 GeV/c, The direct photon v_3 is consistent with that for hadrons over the entire p_T range.

We compare the data to several recent calculations, which treat the direct photon yields and the azimuthal asymmetries in a consistent production and evolution framework. None of them describe the full systematics of the data adequately, but there has been progress in the last few years. The general trend of the models appears to be including sources from the earliest (pre-equilibrium, see for instance Ref. [15]) or very late times in the evolution of the system, while giving less emphasis to photon production at intermediate times, when most of the expansion occurs. PHSD includes new sources from the HG and photon production even after the hadrons are decoupled from each other, which improves description of the yields but still under predicts v_2. The model that best approximates the measured v_2, including the p_T region where v_2 reaches its maximum value, starts the evolution with a large initial boost even before thermalization [12]. It is also worth noting that the microscopic transport model [13] is able to describe the anisotropies as well as the full-scale viscous hydrodynamics [14].

While the data are getting more differential and more accurate, and model calculations improve, the "direct photon puzzle" remains unresolved. High-quality data of yields and v_2 and v_3 for different collision systems, including very asymmetric ones, and energies would help to further improve our understanding of direct photon production because robust models must be able to describe the data over a wide range of experimental conditions.

ACKNOWLEDGMENTS

We thank the staff of the Collider-Accelerator and Physics Departments at Brookhaven National Laboratory and the staff of the other PHENIX participating institutions for their vital contributions. We acknowledge support from the Office of Nuclear Physics in the Office of Science of the Department of Energy, the National Science Foundation, the Abilene Christian University Research Council, the Research Foundation of SUNY, and the Dean of the College of Arts and Sciences, Vanderbilt University (U.S.A); the Ministry of Education, Culture, Sports, Science, and Technology and the Japan Society for the Promotion of Science (Japan); the Conselho Nacional de Desenvolvimento Científico e Tecnológico and the Fundação de Amparo à Pesquisa do Estado de São Paulo (Brazil); the Natural Science Foundation of China (People's Republic of China); the Croatian Science Foundation and the Ministry of Science, Education, and Sports (Croatia); the Ministry of Education, Youth and Sports (Czech Republic); the Centre National de la Recherche Scientifique, the Commissariat à l'Énergie Atomique, and the Institut National de Physique Nucléaire et de Physique des Particules (France); the Bundesministerium für Bildung und Forschung, the Deutscher Akademischer Austausch Dienst, and the Alexander von Humboldt Stiftung (Germany); the National Science Fund, OTKA, Károly Róbert University College, and the Ch. Simonyi Fund (Hungary); the Department of Atomic Energy and the Department of Science and Technology (India); the Israel Science Foundation (Israel); the Basic Science Research Program through the NRF of the Ministry of Education (Korea); the Physics Department, Lahore University of Management Sciences (Pakistan); the Ministry of Education and Science, Russian Academy of Sciences, Federal Agency of Atomic Energy (Russia); VR and the Wallenberg Foundation (Sweden); the U.S. Civilian Research and Development Foundation for the Independent States of the Former Soviet Union; the Hungarian American Enterprise Scholarship Fund; and the U.S.-Israel Binational Science Foundation.

[1] E. V. Shuryak, Quark-gluon plasma and hadronic production of leptons, photons, and pions, Phys. Lett. B **78**, 150 (1978).

[2] A. Adare *et al.* (PHENIX Collaboration), Enhanced Production of Direct Photons in Au + Au Collisions at $\sqrt{s_{NN}} = 200$ GeV and Implications for the Initial Temperature, Phys. Rev. Lett. **104**, 132301 (2010).

[3] A. Adare *et al.* (PHENIX Collaboration), Centrality dependence of low-momentum direct-photon production in Au + Au collisions at 200 GeV, Phys. Rev. C **91**, 064904 (2015).

[4] A. Adare *et al.* (PHENIX Collaboration), Observation of Direct-Photon Collective Flow in Au + Au Collisions at $\sqrt{s_{NN}} =$ 200 GeV, Phys. Rev. Lett. **109**, 122302 (2012).

[5] A. Adare *et al.* (PHENIX Collaboration), Measurement of Higher Order Flow Harmonics in Au + Au Collisions at $\sqrt{s_{NN}} = 200$ GeV, Phys. Rev. Lett. **107**, 252301 (2011).

[6] M. Wilde (ALICE Collaboration), Measurement of direct photons in *pp* and PbPb collisions with ALICE, Nucl. Phys. A **904**, 573c (2013).

[7] D Lohner (ALICE Collaboration), Measurement of direct-photon elliptic flow in Pb-Pb collisions at $\sqrt{s_{NN}} = 2.76$ TeV, J. Phys.: Conf. Ser. **446**, 012028 (2013).

[8] S. Turbide, C. Gale, and R. J. Fries, Azimuthal Asymmetry of Direct Photons in High Energy Nuclear Collisions, Phys. Rev. Lett. **96**, 032303 (2006).

[9] R. Chatterjee, E. S. Frodermann, U. Heinz, and D. K. Srivastava, Elliptic Flow of Thermal Photons in Relativistic Nuclear Collisions, Phys. Rev. Lett. **96**, 202302 (2006).

[10] R. Chatterjee and D. K. Srivastava, Elliptic flow of thermal photons and formation time of the quark gluon plasma at energies available at the BNL Relativistic Heavy Ion Collider (RHIC), Phys. Rev. C **79**, 021901 (2009).

[11] K. Dusling, Photons as a viscometer of heavy ion collisions, Nucl. Phys. A **839**, 70 (2010).

[12] H. van Hees, C. Gale, and R. Rapp, Thermal photons and collective flow at energies available at the BNL Relativistic Heavy-Ion Collider, Phys. Rev. C **84**, 054906 (2011).

[13] O. Linnyk, W. Cassing, and E. L. Bratkovskaya, Centrality dependence of the direct-photon yield and elliptic flow in heavy-ion collisions at $\sqrt{s_{NN}} = 200$ GeV, Phys. Rev. C **89**, 034908 (2014).

[14] C. Gale, Y. Hidaka, S Jeon, S. Lin, J.-F. Paquet, R. D. Pisarski, D. Satow, V. V. Skokov, and G. Vujanovic, Production and Elliptic Flow of Dileptons and Photons in a Matrix Model of the Quark-Gluon Plasma, Phys. Rev. Lett. **114**, 072301 (2015).

[15] B. Muller, S.-Y. Wu, and D.-L. Yang, Elliptic flow from thermal photons with magnetic field in holography, Phys. Rev. D **89**, 026013 (2014).

[16] C. Shen, U. Heinz, J.-F. Paquet, and C. Gale, Thermal photons as a quark-gluon plasma thermometer revisited, Phys. Rev. C **89**, 044910 (2014).

[17] C. Shen, U. Heinz, J.-F. Paquet, I. Kozlov, and C. Gale, Anisotropic flow of thermal photons as a quark-gluon plasma viscometer, Phys. Rev. C **91**, 024908 (2015).

[18] H. van Hees, M. He, and R. Rapp, Pseudo-critical enhancement of thermal photons in relativistic heavy-ion collisions? Nucl. Phys. A **933**, 256 (2015); (private communication).

[19] A. Monnai, Thermal photon v_2 with slow quark chemical equilibration, Phys. Rev. C **90**, 021901 (2014).

[20] R. Chatterjee, H. Holopainen, I. Helenius, T. Renk, and K. J. Eskola, Elliptic flow of thermal photons from an event-by-event hydrodynamic model, Phys. Rev. C **88**, 034901 (2013).

[21] M. Dion, J.-F. Paquet, B. Schenke, C. Young, S. Jeon, and C. Gale, Viscous photons in relativistic heavy ion collisions, Phys. Rev. C **84**, 064901 (2011).

[22] F.-M. Liu and S.-X. Liu, Quark-gluon plasma formation time and photons from heavy ion collisions, Phys. Rev. C **89**, 034906 (2014).

[23] G. Vujanovic *et al.*, Probing the early-time dynamics of relativistic heavy-ion collisions with electromagnetic radiation, Nucl. Phys. A **932**, 230 (2014).

[24] L. McLerran and B. Schenke, The Glasma, photons and the implications of anisotropy, Nucl. Phys. A **929**, 71 (2014).

[25] K. Tuchin, Electromagnetic radiation by quark-gluon plasma in a magnetic field, Phys. Rev. C **87**, 024912 (2013).
[26] L. McLerran and B. Schenke, A tale of tails: Photon rates and flow in ultra-relativistic heavy ion collisions, Nucl. Phys. A **946**, 158 (2016).
[27] G. Basar, D. E. Kharzeev, and V Skokov, Conformal Anomaly as a Source of Soft Photons in Heavy Ion Collisions, Phys. Rev. Lett. **109**, 202303 (2012).
[28] F. Gelis, H. Niemi, P. V. Ruuskanen, and S. S. Rasanen, Photon production from non-equilibrium QGP in heavy-ion collisions, J. Phys. G **30**, S1031 (2004).
[29] T. S. Biro, Zs. Szendi, and Zs. Schram, Illusory flow in radiation from accelerating charge, Eur. Phys. J. A **50**, 62 (2014).
[30] Y. Hidaka, S. Lin, R. Pisarski, and D. Satow, Dilepton and photon production in the presence of a nontrivial Polyakov loop, J. High Energy Phys. 10 (2015) 005.
[31] S. Campbell, Photon production from gluon-mediated quark–anti-quark annihilation at confinement, Phys. Rev. C **92**, 014907 (2015).
[32] M. Allen *et al.*, PHENIX inner detectors, Nucl. Instrum. Methods Phys. Res., Sect. A **499**, 549 (2003).
[33] W. Anderson *et al.*, Design, construction, operation and performance of a hadron blind detector for the PHENIX experiment, Nucl. Instrum. Methods Phys. Res., Sect. A **646**, 35 (2011).
[34] K. Adcox *et al.*, PHENIX central arm tracking detectors, Nucl. Instrum. Methods Phys. Res., Sect. A **499**, 489 (2003).
[35] M. Aizawa *et al.*, PHENIX central arm particle I.D. detectors, Nucl. Instrum. Methods Phys. Res., Sect. A **499**, 508 (2003).
[36] L. Aphecetche *et al.*, The PHENIX calorimeter, Nucl. Instrum. Methods Phys. Res., Sect. A **499**, 521 (2003).
[37] S. Afanasiev *et al.* (PHENIX Collaboration), Measurement of Direct Photons in Au + Au Collisions at $\sqrt{s_{NN}} = 200$ GeV, Phys. Rev. Lett. **109**, 152302 (2012).
[38] A. Adare *et al.*, Suppression Pattern of Neutral Pions at High Transverse Momentum in Au + Au Collisions at $\sqrt{s_{NN}} =$ 200 GeV and Constraints on Medium Transport Coefficients, Phys. Rev. Lett. **101**, 232301 (2008).
[39] E. Richardson *et al.*, A reaction plane detector for PHENIX at RHIC, Nucl. Instrum. Methods Phys. Res., Sect. A **636**, 99 (2011).
[40] A. M. Poskanzer and S. A. Voloshin, Methods for analyzing anisotropic flow in relativistic nuclear collisions, Phys. Rev. C **58**, 1671 (1998).
[41] A. Adare *et al.* (PHENIX Collaboration), Azimuthal anisotropy of π^0 and η mesons in Au + Au collisions at $\sqrt{s_{NN}} = 200$ GeV, Phys. Rev. C **88**, 064910 (2013).
[42] A. Adare *et al.* (PHENIX Collaboration), Measurement of the higher-order anisotropic flow coefficients for identified hadrons in Au + Au collisions at $\sqrt{s_{NN}} = 200$ GeV, Phys. Rev. C **93**, 051902 (2016).
[43] A. Adare *et al.* (PHENIX Collaboration), Deviation from quark-number scaling of the anisotropy parameter v_2 of pions, kaons, and protons in Au + Au collisions at $\sqrt{s_{NN}} = 200$ GeV, Phys. Rev. C **85**, 064914 (2012).
[44] A. Adare *et al.*, Scaling Properties of Azimuthal Asymmetry in Au + Au and Cu + Cu Collisions at $\sqrt{s_{NN}} =$ 200 GeV, Phys. Rev. Lett. **98**, 162301 (2007).
[45] S. S. Adler *et al.* (PHENIX Collaboration), Measurement of Direct Photon Production in $p + p$ Collisions at $\sqrt{s_{NN}} = 200$ GeV, Phys. Rev. Lett. **98**, 012002 (2007).
[46] S. Ryu, J. F. Paquet, C. Shen, G. S. Denicol, B. Schenke, S. Jeon, and C. Gale, The Importance of the Bulk Viscosity of QCD in Ultrarelativistic Heavy-Ion Collisions, Phys. Rev. Lett. **115**, 132301 (2015).
[47] J.-F. Paquet, C. Shen, G. S. Denicol, M. Luzum, B. Schenke, S. Jeon, and C. Gale, The production of photons in relativistic heavy-ion collisions, Phys. Rev. C **93**, 044906 (2016); J.-F. Paquet (private communication).
[48] C. Shen, J.-F. Paquet, U. Heinz, and C. Gale, Photon emission from a momentum anisotropic quark-gluon plasma, Phys. Rev. C **91**, 014908 (2015).
[49] O. Linnyk, V. Konchakovski, T. Steinert, W. Cassing, and E. L. Bratkovskaya, Hadronic and partonic sources of direct photons in relativistic heavy-ion collisions, Phys. Rev. C **92**, 054914 (2015); (private communication).